ORIGINAL PAPER

Mixed-mode crack growth in ductile thin-sheet materials under combined in-plane and out-of-plane loading

J.-H. Yan · M. A. Sutton · X. Deng · Z. Wei · Pablo Zavattieri

Abstract Ductile thin-sheet structures, such as fuse-lage skin or automobile panels, are widely used in engineering applications. These structures often-times are subjected to mixed mode (I/II/III) load-ing, with stable crack growth observed prior to final fracture. To characterize specific specimen deforma-tions during stable tearing, a series of mixed-mode I/III stable tearing experiments with highly ductile thin-sheet aluminum alloy and steel specimens have been measured by using three-dimensional digital image correlation (3D-DIC). Measurements include (a) spec-imen's deformed shape and 3D full-field surface dis-placement fields, (b) load-crack extension response and (c) crack path during stable tearing, (d) angular and radial distributions of strains and (e) the mixed mode crack-opening displacement (COD, measured at 1- mm from crack tip along crack surface) variation as a func-tion of crack extension. Results indicate that for both aluminum alloy and steel at all mixed-mode I/III load-ing conditions ($\Phi = 30°$, $60°$ and $90°$), the crack tip fields have almost identical angular and radial polar strain distributions. The mixed mode I/III fields were different from those observed for the nominal Mode I loading case ($\Phi = 0°$). The effect of the Mode III loading component is that it lowers the magnitude of the dominant strain component $\varepsilon_{\theta\theta}$ ahead of the grow-ing crack tip and increases the singularity of the strain as compared with that in the mode I case. In addition, measurements indicate that the average mixed mode I/III stable COD for AL6061-T6 (GM6208 steel) is $4\times(3\times)$ greater than the average Mode I stable COD.

1 Introduction

Most often components of an actual machine or struc-ture, especially those which contain thin sheet mate-rial such as fuselage or automobile panels, undergo complex loading in service conditions involving a com-bination of tension (mode I), in-plane shear (mode II) and out-of-plane shear (mode III; Paterson and Gungor 1997; Gao and Shih 1998; Jones et al. 2001; Kamat and Hirth 1995; Kamat et al. 1998; Lan et al. 2006; Liu et al. 2004; Pan 1990). A crack in such a component is therefore likely to be subjected to mixed mode loading conditions at the crack front, and stable crack growth (SCG) in ductile materials generally is observed prior to final fracture. Understanding the crack growth pro-cess under mixed mode conditions in ductile materials

J.-H. Yan (✉) · M. A. Sutton · X. Deng · Z. Wei
Department of Mechanical Engineering,
University of South Carolina, Columbia, SC 29208, USA
e-mail: yan@cec.sc.edu

P. Zavattieri
GM Research and Development Center, Warren,
MI 48090, USA

is an important aspect of structural integrity analysis, especially for thin-sheet structures.

Mixed-mode I/III fracture has been the focus of many investigations (Pan 1990; Pan and Shih 1992; Paterson and Gungor 1997; Gao and Shih 1998; Jones et al. 2001; Kamat and Hirth 1995; Kamat et al. 1998; Liu et al. 2004; Zucchini et al. 2000; Sutton et al. 2001; Yan et al. 2007; Wei et al. 2005; Wei 2008), with most of the work focused on fracture toughness measurements and evaluation (Jones et al. 2001; Kamat and Hirth 1995; Kamat et al. 1998; Li et al. 1998) instead of on stable tearing of thin sheet materials under mixed mode I/III loading. Mixed mode I/III fracture in ductile thin sheet materials is quite complex, including large scale yielding, significant warping of the specimen (Wei et al. 2005; Sutton et al. 2001; Yan et al. 2007; Sutton et al. 2007) and a highly three-dimensional (3D) response of the flawed component, resulting in complex stress and strain fields near the crack tip (Wei et al. 2005; Zucchini et al. 2000; Sutton et al. 2001; Pan 1990; Pan and Shih 1992). This situation has led to limited reports of experimental investigations and numerical simulations regarding crack growth under mixed mode I/III loading in the literature (Paterson and Gungor 1997; Wei et al. 2005; Sutton et al. 2001, 2007; Yan et al. 2007; Wei 2008).

Crack tip fields play a significant role in understanding the crack behavior and the fracture process in thin structure under mixed-mode I/III loading conditions. Characterizing the crack tip fields is also necessary to develop a general mixed-mode fracture criterion in ductile materials. Under conditions of small-scale yielding and small deformation, and neglecting through-thickness variations, Pan (1990), Pan and Shih (1992), and Gao and Shih (1998) performed elastic-plastic asymptotic analyses of mixed mode I/III crack-tip fields for a stationary crack. Related finite element solutions indicate that within the plastic zone, the in-plane stresses are more singular than the out-of-plane shear stresses. Over a certain distance, the near tip in-plane stress can be said to be more singular than $r^{1/(n+1)}$ while the near-tip out-of-plane shear stress is less singular than $r^{1/(n+1)}$, where r is the radial distance to the tip and n is the strain hardening exponent of the material.

With the development of three-dimensional (3D) digital image correlation, a technique capable of measuring full-field 3D surface displacements in the presence of large out-of-plane warping, the authors recently studied the crack tip field characteristics of stationary cracks under quasi-static mixed mode I/III loading in thin sheet ductile aluminum alloy and steel by using 3D-DIC (Yan et al. 2007). The data on strain fields in both AL6061-T6 aluminum alloy and GM6208 steel consistently show that for a given strain component, the normalized angular and radial strains at all load levels can be reasonably represented by a single functional form over the range of loading considered, confirming that the strain fields in highly ductile thin-sheet material undergoing combined in-plane tension and out-of-plane shear loading can be expressed in terms of separable angular and radial functions. However, for a growing crack in thin sheet ductile materials under mixed mode I/III loading, reports on crack tip displacement and strain fields (in particular on the angular and radial distributions of strains) are rare; only preliminary results are available on crack tip fields for 2.3 mm thick AL2024-T3 aluminum alloy under tension-torsion loading and for 2 mm thick AL6061-T6 aluminum alloy under impact and quasi-static mixed mode I/III loading (Sutton et al. 2001, 2007). In their experimental investigation of crack growth in thin sheet 2024-T3 aluminum alloy under tension-torsion loading, Sutton et al. (2001) obtained the surface strain fields right after the initial crack growth in tension-torsion specimen at a tension/torsion ratio of 3.32 with the help of 3D DIC. They observed that there was coupling of in-plane deformations with the out-of-plane displacement. It is also shown that the surface strains (ε_{xx}, ε_{xy} and ε_{yy}) was less than 0.06 just after the onset of crack growth in the tension-torsion specimen. However, much higher strain values ahead of a growing crack (with a crack extension of about 10–13 mm) were reported in 2 mm thick AL6061-T6 aluminum alloy under impact and quasi-static mixed mode I/III loading, where a different loading fixture with much larger out-of-plane motion was used as compared to those by Sutton et al. (2001). It is noted that the authors did not report on either the angular or radial distributions of strain ahead of a growing crack which need to be quantitatively characterized. Therefore, how the crack tip strain fields will vary with the crack extension is still an open issue in the mixed mode I/III fracture especially for ductile thin sheet materials.

Due to the complexity of the fracture process accompanied by large deformation and large-scale yielding that develops in ductile materials under mixed mode I/III loading, there is currently no general fracture criterion available for mixed mode fracture of thin sheet

ductile materials. A critical mixed mode I/II COD (crack opening displacement measured at 1-mm from crack tip along crack surface, in some of the previous literature, crack tip opening displacement (CTOD) measured at 1-mm from crack tip like the use of COD in the present paper was used) has been shown to be a viable crack growth criterion for many ductile materials, including 2024-T3 aluminum alloy, under combined tension (mode I) and in-plane shear (mode II) loading conditions (Ma et al. 1999; Newman et al. 2003; Sutton et al. 2000a,b). A generalized form of COD might also be able to explain and predict both the instant and direction of crack growth when a ductile material is subjected to nominally mixed mode I/III conditions (Wei et al. 2005). However, only limited data exists regarding the evolution of COD under nominally mixed mode I/III loading. As noted by Sutton et al. (2001), the measured critical COD for tension-torsion loading (a) is ~8% larger than observed for in-plane tension-shear and (b) is approximately constant for crack extension, $\Delta a > 3t$, where t is the specimen thickness. Recently, the authors quantified COD in a more ductile aluminum alloy under impact and quasi-static mixed mode I/III loading (Sutton et al. 2007). The measured stable COD under combined mode I/III loading was found to be nearly four times larger than observed during mixed mode I/II or mode I fracture of the same material. The discrepancy in COD data under mixed mode I/III loading indicates that the critical COD has dependence on mixed mode type.

In the current study, full field deformation measurements using 3D DIC on a series of mixed-mode I/III fracture experiments with crack growth on highly ductile, thin aluminum alloy and steel specimens are used to characterize the crack tip fields and COD variation during stable tearing. Key results from these analyses are presented, including (a) 3D full-field surface displacement fields, (b) angular and radial distribution of strain, (c) crack path and load versus crack extension data, and (d) critical generalized COD measurements as a function of crack extension.

2 Experimental conditions and procedures

### 2.1 Test materials, specimens and setup for mixed mode I/III experiments

Aluminum alloy AL6061-T6 and GM6208 steel specimens fabricated from 2 mm thick sheet material are used as test materials in this study. Their uniaxial true stress-strain curves and the corresponding Ramberg–Osgood relationships were reported previously (Yan et al. 2007) and are summarized in Table 1, where E is the Young's modulus, $\sigma_{0.2}$ is the engineering yield strength that is also used as a reference stress in Ramberg–Osgood relationships, σ_b is the engineering ultimate tensile strength, ν is Poisson's ratio, $\varepsilon_0 = \sigma_{0.2}/E$ is a reference strain, n and α are the strain hardening exponent and the strain hardening coefficient in the Ramberg–Osgood relation. According to solutions by Hutchinson (1968) and Rice and Rosengren (1968) (HRR solutions), the singularity of strain ahead of a stationary crack is a function of the strain hardening coefficient n in the Ramberg–Osgood relation.

Figure 1 shows the in-plane dimensions for the 2 mm thick, single-edged mixed mode I/III fracture specimens. The aluminum alloy and steel specimens are laser cut with a notch length of 28.6 mm and an in-plane width of 63.5 mm. All specimens are oriented in the LT direction (i.e. crack is aligned with the transverse direction and perpendicular to the sheet's rolling direction).

It should be pointed out that in the current study, specimens with in-plane dimension of 63.5 mm (w) × 76.2 mm (h) shown in Fig. 1 were employed for both AL6061-T6 and GM6208 steel, while in our previous study (Yan et al. 2007), specimens with in-plane dimension of 76.2 mm(w) × 76.2 mm (h) were used for AL6061-T6, and 63.5 mm (w) × 76.2 mm (h) specimens for GM6208 steel. No significant changes were observed in the crack tip strain fields between wide and narrow AL6061-T6 specimens under loading angle of

Table 1 Material properties for AL6061-T6 and GM6208 steel

Materials	E (GPa)	$\sigma_{0.2}$(MPa)	σ_b(MPa)	Maximum elongation	ν	n	α	ε_0
AL6061-T6	70.3	332	350	0.106	0.33	13.1	2.84	0.00473
GM6208	198.0	339	418	0.468	0.33	5.0	13.11	0.00172
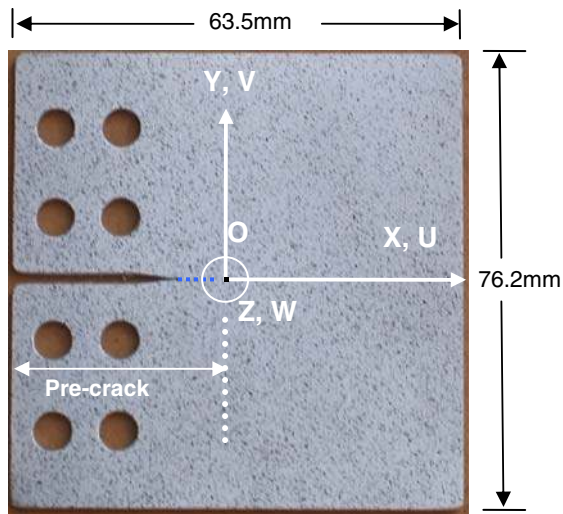
Fig. 1 In-plane specimen dimensions and the global coordinate system for mixed I/III mode experiments. The origin O is at the fatigue pre-crack tip. The specimen thickness is 2 mm

$\Phi = 0°$, $30°$ and $90°$, with only a slight change in crack path for $\Phi = 60°$ in the AL6061-T6 specimen.

Figure 2 illustrates a setup of quasi-static mixed I/III mode experiments at the loading angle $\Phi = 60°$ with a 3D displacement measurement system. Remote Mode I Mode III loading cases correspond to loading angles $\Phi = 0°$ and $\Phi = 90°$, respectively. Detailed information regarding the loading fixture can be found in Yan et al. (2007). It should be pointed out that the extension bar (item 10 in Fig. 2) was used to increase the space between the specimen and the upper hydraulic grip so that the 3D displacement measurement system can be constructed for mixed mode I/III experiments at loading angles $\Phi = 60°$ and $\Phi = 90°$. Mixed mode I/III experiments are performed using a MTS 810 test machine under displacement-controlled conditions. The loading rate for a typical specimen is 0.04 mm/s. During the experiment, rotation of the lower (moving) grip around the loading axis was fully constrained using a specially designed constraint mechanism (see item 9 in Fig. 2).

The 3D digital image correlation (DIC) system for the mixed mode I/III experiments shown in Fig. 2 was composed of two Q-Imaging QICAM digital cameras with a CCD resolution of 1,392 × 1,040 pixels, a sensor pixel size of 4.65 μm × 4.65 μm and 12 bits for intensity resolution. Due to space restrictions introduced by the physical location of the MTS support columns and

the hydraulic grips, the pan angle between the two cameras in the stereovision system was limited to < 20°. Both cameras were mounted to a rigid cross-member in order to minimize relative motion between the two cameras during the experiment. The cross-member was mounted to a three-axis translation stage so that the camera system could be moved to retain focus during the experiments, especially for our relatively high magnification setup.

Nikon AF Nikkor 28 and 200 mm f/2.8D lenses are used in the experiments. The distance between the camera and the specimen was ≈350 mm for the experiments. Two sets of experiments were performed to obtain global and local crack tip measurements. Typical magnification factors are 21 pixels/mm for the low magnification experiments (to measure overall deformations and shape of the specimen) and 80 pixels/mm for the high magnification experiments (to improve the accuracy of crack tip COD measurements).

Since substantial motion of the sample occurred during mixed mode I/III loading, the lenses were selected to ensure that the expected maximum out of plane motions stay within the depth of field for the experimental arrangement. For the low magnification camera arrangement, the depth of field was 30–40 mm. For these experiments, the out of plane displacements were measured to be less than 25 mm for all loading cases. Thus, based on the measurements, the stereovision arrangement was configured with a sufficient depth-of field so that blurring/defocusing was not present and hence did not affect the measurement process. It is noted that, for a higher magnification camera configuration used to measure COD closer to the crack tip, the depth of field is much smaller so that the three-axis translation stage shown in Fig. 2 is used to trace the crack tip region and to focus both cameras on this region.

2.2 Experimental procedures

The following outline is typical for mixed mode I/III experiments that employ a stereo-vision system to acquire full-field deformations.

(1) All specimens are fatigue pre-cracked under nominally Mode I conditions to produce a sharp crack tip for subsequent mixed-mode I/III fracture experiments. The total fatigue pre-crack length is controlled to be 33 ± 1 mm for all specimens.

Fig. 2 The setup of quasi-static mixed I/III mode experiments with a 3D full-field surface displacement measurement system
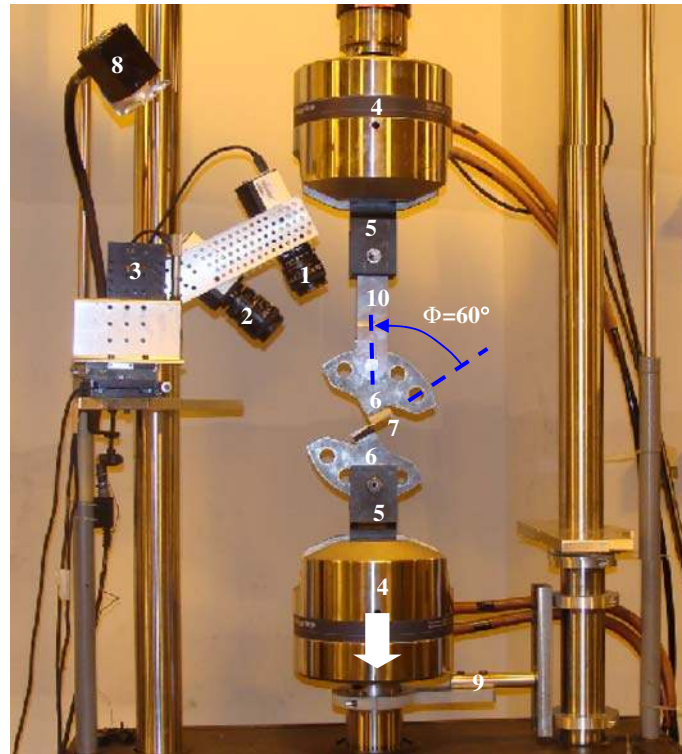
1—Camera 0, 2—Camera 1, 3—Translation Stage, 4—Hydraulic Grip 5—Clevis, 6—Fixture, 7—Specimen, 8—Light Source, 9-Rotation Constraint, 10—extension bar

(2) Prior to performing each mixed mode I/III experiment, the specimen is lightly coated to obtain a random black-and-white speckle pattern having a spatial variation in intensity that is appropriate for displacement measurement using computer vision. In order to improve the bonding between the coating and the specimen, a Rust-Oleum Specialty High Heat White enamel spray paint and Rust-Oleum® Stops Rust Flat Black enamel spray paint were adopted for the speckle pattern on all specimens.

(3) For a given loading angle Φ, the painted mixed mode I/III specimen is mounted to the loading fixture, and the mixed mode I/III experiment was set up with the 3D DIC system as shown in Fig. 2.

(4) The pan angle between the two cameras is adjusted so that the area of interest on the front surface of the specimen can be captured by both cameras. Both cameras are adjusted so that they are well focused on the front surface of the specimen.

(5) The loading fixture with the specimen is removed, the two cameras are synchronized, and the stereovision system is calibrated according to the procedures outlined in Sutton et al. (2007) and Yan et al. (2007). From the calibration results, the measurement precision is estimated to 0.0012 mm for the in-plane displacement measurement and 0.0097 mm for the out-of-plane displacement measurement for a typical mixed mode I/III experiment setup with the image scale factor being about 25 pixel/ mm (Yan et al. 2007).

(6) The loading fixture with the specimen is re-installed in the loading system. Prior to loading the specimen, several un-deformed image pairs of the specimen is acquired and one of the pairs is used (a) as the reference image pair for future deformation measurements and (b) to determine the initial shape of the specimen.

(7) The specimen is loaded in displacement control at 0.04 mm/s, and synchronize image pairs of the specimen's front surface are acquired in a
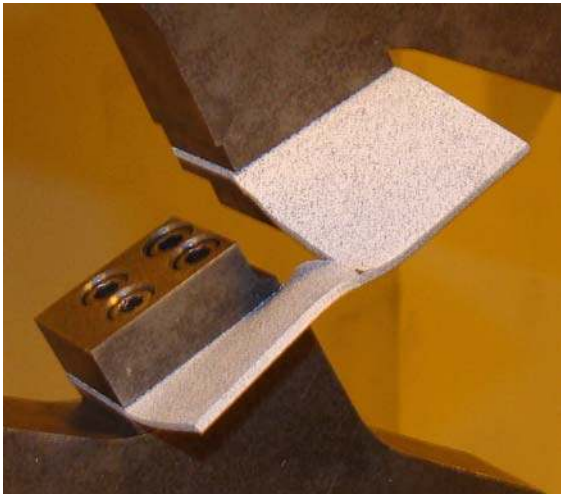
Fig. 3 The deformed shape of an AL6061-T6 specimen with about 20 mm crack extension during a mixed mode I/III experiment at loading angle $\Phi = 60°$

time-controlled mode during loading (typically every 2 s for one image pair) while both the load and far-field grip displacements are recorded during the image acquisition process.

In this study, results are reported for loading angles $\Phi = 0°, 30°, 60°$ and $90°$ in the mixed mode I/III experiments of aluminum alloy and steel specimens. It should be pointed out that the camera system must be removed, reconfigured, remounted and recalibrated for each different loading angle used to perform an experiment.

3 Experimental results and discussion

3.1 Shape of deformed specimens during crack growth

Figure 3 shows a typical deformed shape of an AL-6061-T6 specimen during a mixed mode I/III experiment at loading angle $\Phi = 60°$ when crack extension was about 20 mm. As can be seen from the figure, the deformation of the specimen undergoing mixed mode I/III crack growth is complex, with a large out-of-plane warping and curvature.

To characterize the deformation during mixed mode I/III experiments by DIC, the Cartesian coordinate system shown in Fig. 1 is used to define displacement and strain components. Since all displacements and

strains in DIC are calculated based on the un-deformed image configuration (the initial configuration), a reference coordinate system is shown in Fig. 1, which is used for measurement data analysis. The origin of the coordinate is at the pre-crack tip, the X-axis is along the pre-crack direction, the Y-axis is perpendicular to the crack direction and directed towards the stationary grip (the upper grip in Fig. 2), and the Z-axis is perpendicular to the $X - Y$ plane, which is the underformed specimen surface. Also shown in the figure, U, V and W denote the specimen's surface displacement components in the X, Y and Z directions, respectively.

From DIC measurements, representative 3D deformed specimen configurations at loading angles $\Phi = 0°, 30°, 60°, 90°$ in quasi-static mixed-mode I/III experiments with crack extension around 10 mm are shown in Fig. 4a and b. As shown in the figures, even for the nominal tension (mode I) loading, the deformed specimen shape under static loading is complex and fully three-dimensional in shape with a noticeable out-of-plane displacement due to crack slanting (in AL6061-T6) and a substantial through-thickness dimpling with far-field warping (in GM6208 steel). Compared with $\Phi = 0°$, increased out-of-plane displacement and specimen curvature are clearly visible as the applied loading angle Φ increases. It is noted that the deformed shape at a given $\Phi \geq 0°$ is similar for both AL6061-T6 and GM6208 steel specimen, although AL6061-T6 specimen has less deformation and far-field warping compared to the steel specimen.

3.2 Crack paths and load-surface crack extension curves

Figure 5 presents the crack path in the original configuration (e.g. material path) in the $X - Y$ plane for AL6061-T6 and GM6208 specimens loaded at $\Phi = 0°, 30°, 60°$ and $90°$[1] in the stable tearing mixed-mode I/III experiments. As can be seen in Fig. 5, the crack paths in AL6061-T6 specimens at loading angles

---

[1] Mapping from the highly deformed crack positions during stable tearing to the original material points was performed using sequential image analysis, with an estimated accuracy of ± 1 pixel. This is due to the fact that from the digital image correlation process, only the centerpoint data can be obtained by subset matching, so when the subset is approaching the crack tip, we can only get the information at the point half of the subset away from the crack tip.

Fig. 4 Out-of-plane displacement contours for the deformed specimen shapes with various crack extension Δa during quasi-static mixed mode I/III experiments at $\Phi = 0°, 30°, 60°$ and $90°$ for **a** AL6061-T6, **b** GM6208 steel
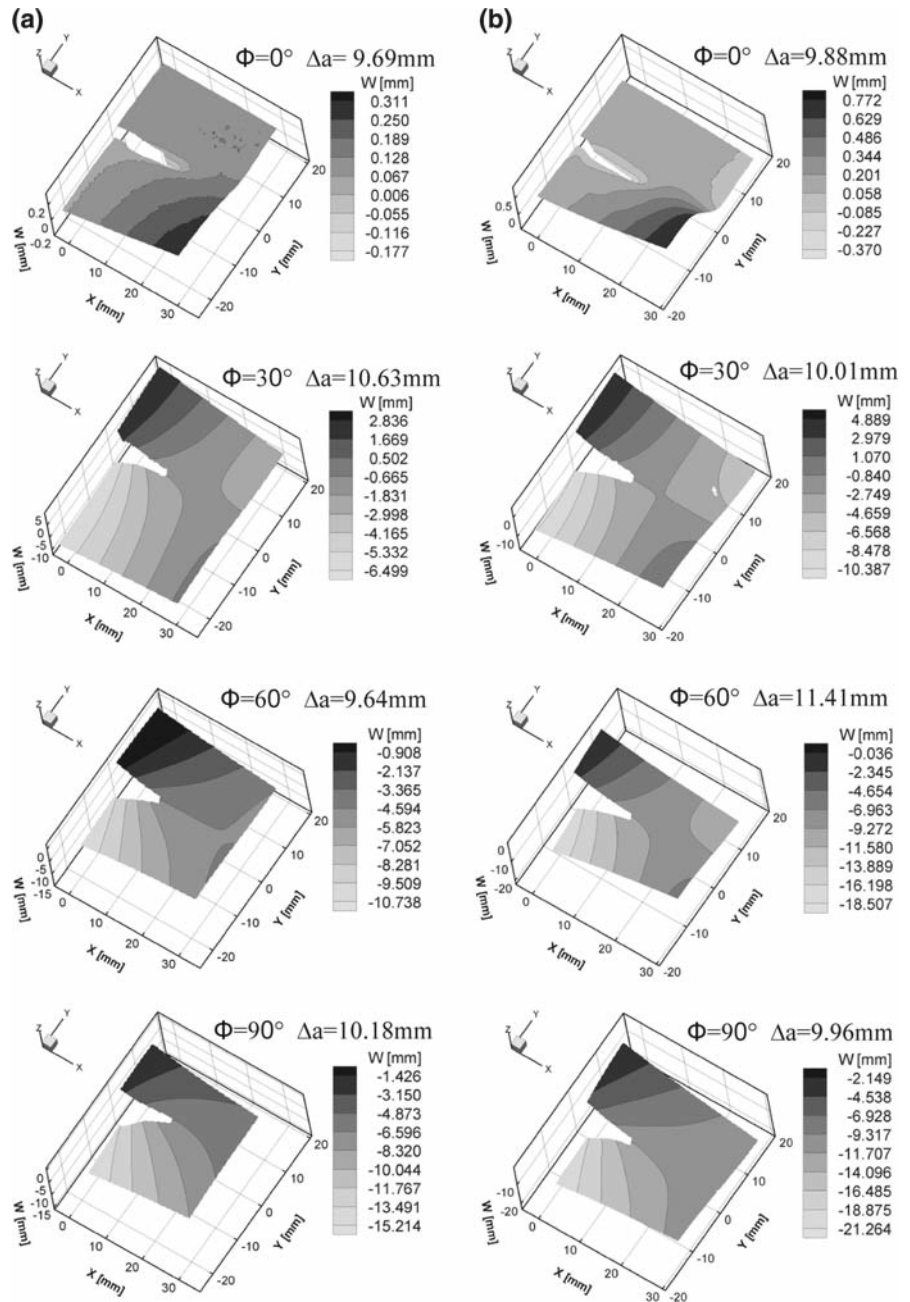
$\Phi = 0°, 30°$ and $60°$ are slightly curved towards the upper (fixed-fixture) portion of the specimen before straightening, with a deviation of about 1 mm (e.g., $t/2$) from the centerline of the specimen. The crack path for $\Phi = 90°$ AL6061-T6 specimen is curved toward the upper (fixed-fixture) portion of the specimen with a maximum deviation ≈ 4.7 mm. The crack paths in

GM6208 steel specimens for $\Phi = 0°, 30°, 60°$ and $90°$ are generally straight and along the centerline of each specimen with deviation around ± 1 mm.

To calculate surface crack extension, the crack tip in each image (corresponding to a specific loading level) was located in the current image and mapped into the original configuration (the reference image). The
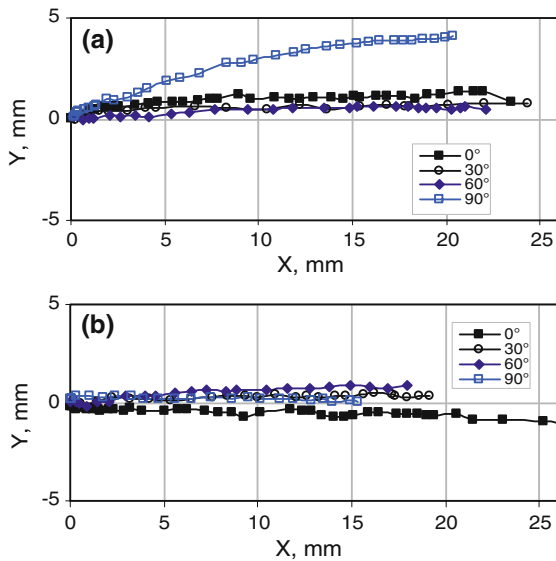
Fig. 5 Crack paths in the un-deformed configuration for **a** AL6061-T6 specimens, **b** GM6208 specimens loaded at $\Phi = 0°$, $30°$, $60°$ and $90°$ in mixed mode I/III experiments

crack extension between any two selected crack tips on the reference image was then computed.[2] The resultant load-surface crack extension curves for AL6061-T6 and GM6208 steel specimens in mixed mode I/III quasi-static experiments are presented in Fig. 6 as a function of the loading angle. It is seen that, (a) for a given material, the maximum load decreases with increasing loading angle Φ; (b) for a given loading angle, the steel specimen has 50% higher maximum load than the aluminum alloy specimen and (c) for each loading angle Φ, stable crack extension occurs prior to the maximum load.

3.3 Displacement fields

3.3.1 AL6061-T6 specimens

Figure 7 presents typical measured components of the surface displacement fields, (U, V, W), for growing cracks in AL6061-T6 specimens during quasi-static mixed mode I/III stable tearing for all four loading angles. As shown in Fig. 7, all three displacement components are non-zero for each loading angle.

For $\Phi = 0°$ (nominally Mode I loading), Fig. 7a shows that the V component is the largest and W is the smallest, with negative values for W around crack tip indicating localized necking/dimpling ahead of the crack, even though the amplitude is small (<0.18 mm).

For $\Phi = 30°$, Fig. 7b indicates that the measured displacement field features are entirely different than those measured for $\Phi = 0°$. Here, W is the largest displacement with U being the smallest. Results also show that the sub-region being imaged undergoes an appreciable 3D rotation during loading, due to both large structural deformations and restricted in-plane grip rotation. The V contour at $\Phi = 30°$ is similar to that at $\Phi = 0°$ in that the lower part (negative Y) moves away from the upper part (positive Y) along the $-Y$ direction, implying separation of the material near the grip region ($X = 0$) along the Y direction during loading.

For $\Phi = 60°$ and $90°$, the U and W displacement fields in Fig. 7c and d are similar to those measured when $\Phi = 30°$. However, the V field is nearly opposite. For material near the grip region ($X = 0$) at $\Phi = 60°$ and $90°$, the lower part (negative Y) moves toward the upper part (positive Y) along the Y direction, implying interference of the material in the wake of crack during I/III loading.

3.3.2 GM6208 steel specimens

For a growing crack undergoing mixed mode I/III loading in GM6208 steel specimens, the typical displacement contours at loading angle of $\Phi = 0°$, $30°$, $60°$ and $90°$ are presented in Fig. 8. As can be seen from Fig. 8, (U, V, W) are present in the displacement fields during mixed mode I/III experiments at all four loading angles. For $\Phi = 0°$, the displacement contours in GM6208 steel specimen are very similar to those in AL6061-T6 specimen; the GM6208 steel specimen has a larger out-of-plane displacement component ($W = -0.38$ mm) near the pre-crack tip at the front surface with respect to the specimen thickness of 2 mm, indicating that substantial dimpling exists ahead of the pre-crack during crack growth, consistent with the observations prior to crack growth (Yan et al. 2007). For $\Phi = 30°$, $60°$ and $90°$, GM6208 steel specimens have deformations that also are consistent with observations for AL6061-T6, i.e., the addition of out-of-plane loading significantly modifies the Mode I component field.

Fig. 6 Load-surface crack extension curves for **a** AL6061-T6 specimens, **b** GM6208 specimens loaded at $\Phi = 0°$, 30°, 60° and 90° in mixed mode I/III experiments. The pre-crack length is about 32.5 mm
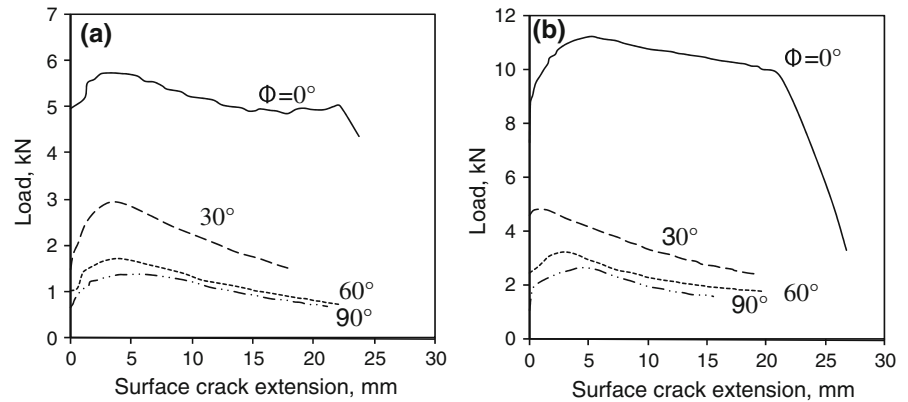
3.4 Angular and radial variations of surface strains

In the computer vision software VIC-3D (Correlated Solutions, Inc 2007), the 3D surface displacement fields were converted to in-plane strain fields in the area of interest using the Lagrangian strain field formulation in terms of the displacement gradients

$$
\varepsilon_{xx} = \partial U/\partial X + \frac{1}{2}\left\{(\partial U/\partial X)^2 + (\partial V/\partial X)^2 + (\partial W/\partial X)^2\right\}
$$

$$
\varepsilon_{yy} = \partial V/\partial Y + \frac{1}{2}\left\{(\partial U/\partial Y)^2 + (\partial V/\partial Y)^2 + (\partial W/\partial Y)^2\right\}
$$

$$
\varepsilon_{xy} = \frac{1}{2}\left\{(\partial U/\partial Y + \partial V/\partial X) + (\partial U/\partial X)(\partial U/\partial Y) + (\partial V/\partial X)(\partial V/\partial Y) + (\partial W/\partial X)(\partial W/\partial Y)\right\} \tag{1}
$$

where (U, V, W) are displacements relative to an (X, Y, Z) coordinate system, respectively, located at the initial fatigue pre-crack tip position (see Fig. 1). The partial derivatives of the displacement field were computed from a polynomial approximation of the displacement in a local neighborhood of 5 points (not pixels). In order to obtain data close to the crack tip, an 11-pixel by 11-pixel subset size with a 2-pixel step size and a 5-point strain window size were used to convert the VIC-3D displacement data into strain components.

To better describe the angular and radial variation of strains, a polar coordinate system is used to define the strain components. The polar coordinate system is shown in Fig. 9 along with the relationship between the polar and global Cartesian systems. The origin of the polar system is the *current* crack tip and the polar angle θ is defined relative to the global X-axis to the radial direction. Strain components (ε_{xx}, ε_{yy} and ε_{xy}) in the original configuration for point M are transformed to the polar coordinate system using Eq. (2). where it is assumed that a planar state exists in the $X - Y$ plane.

$$
\varepsilon_{rr} = \frac{\varepsilon_{xx} + \varepsilon_{yy}}{2} + \frac{\varepsilon_{xx} - \varepsilon_{yy}}{2}\cos(2\theta) + \varepsilon_{xy}\sin(2\theta)
$$

$$
\varepsilon_{\theta\theta} = \frac{\varepsilon_{xx} + \varepsilon_{yy}}{2} - \frac{\varepsilon_{xx} - \varepsilon_{yy}}{2}\cos(2\theta) - \varepsilon_{xy}\sin(2\theta)
$$

$$
\varepsilon_{r\theta} = -\frac{\varepsilon_{xx} - \varepsilon_{yy}}{2}\sin(2\theta) + \varepsilon_{xy}\cos(2\theta) \tag{2}
$$

Figure 10 presents the variations of surface strains as a function of radial distance from the current crack tip (in the un-deformed configuration) in mode I ($\Phi = 0°$) experiments of an AL6061-T6 specimen when the crack extension is $\Delta a = 8.01$ mm and a GM6208 steel specimen when $\Delta a = 3.85$ mm, where the angle $\theta = 0°$ is along the X-axis. Figure 10 shows that the angular distributions for radii $r = 0.5, 0.75$ and 1.0 mm are similar. It is seen that the maximum strain amplitude (especially for $\varepsilon_{\theta\theta}$) increases when r decreases. This is also true for mode I/III loading cases with $\Phi = 30°, 60°$ and 90° in both aluminum alloy and steel specimens. In the remainder of the paper, $r = 0.75$ mm is chosen as the radius when presenting angular variations in strain.

Figure 11 shows the angular and radial variations of the surface strains as a function of crack extension for a growing crack in a mode I ($\Phi = 0°$) AL6061-T6 specimen, where r is the radial distance from the pre-crack tip (in the un-deformed configuration), and
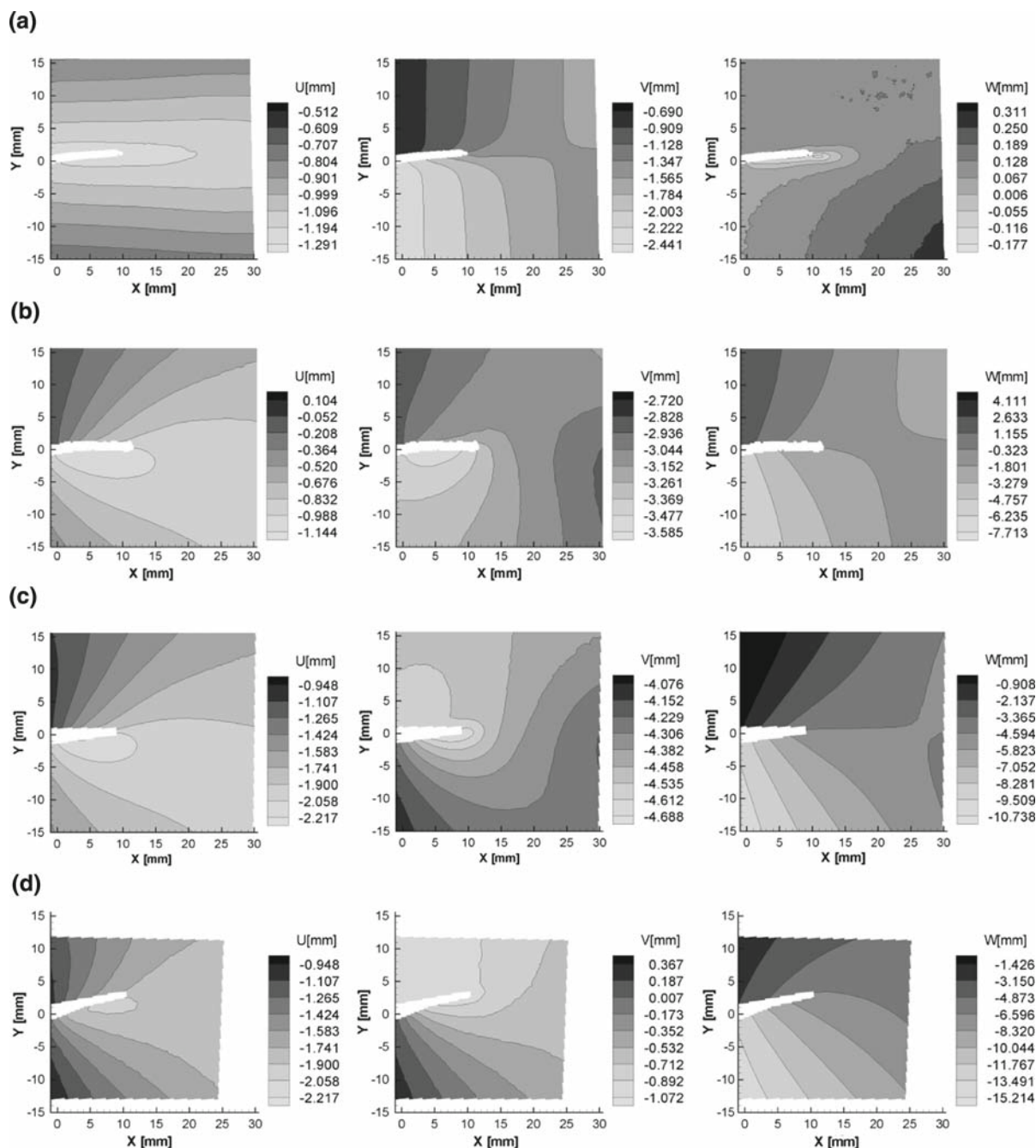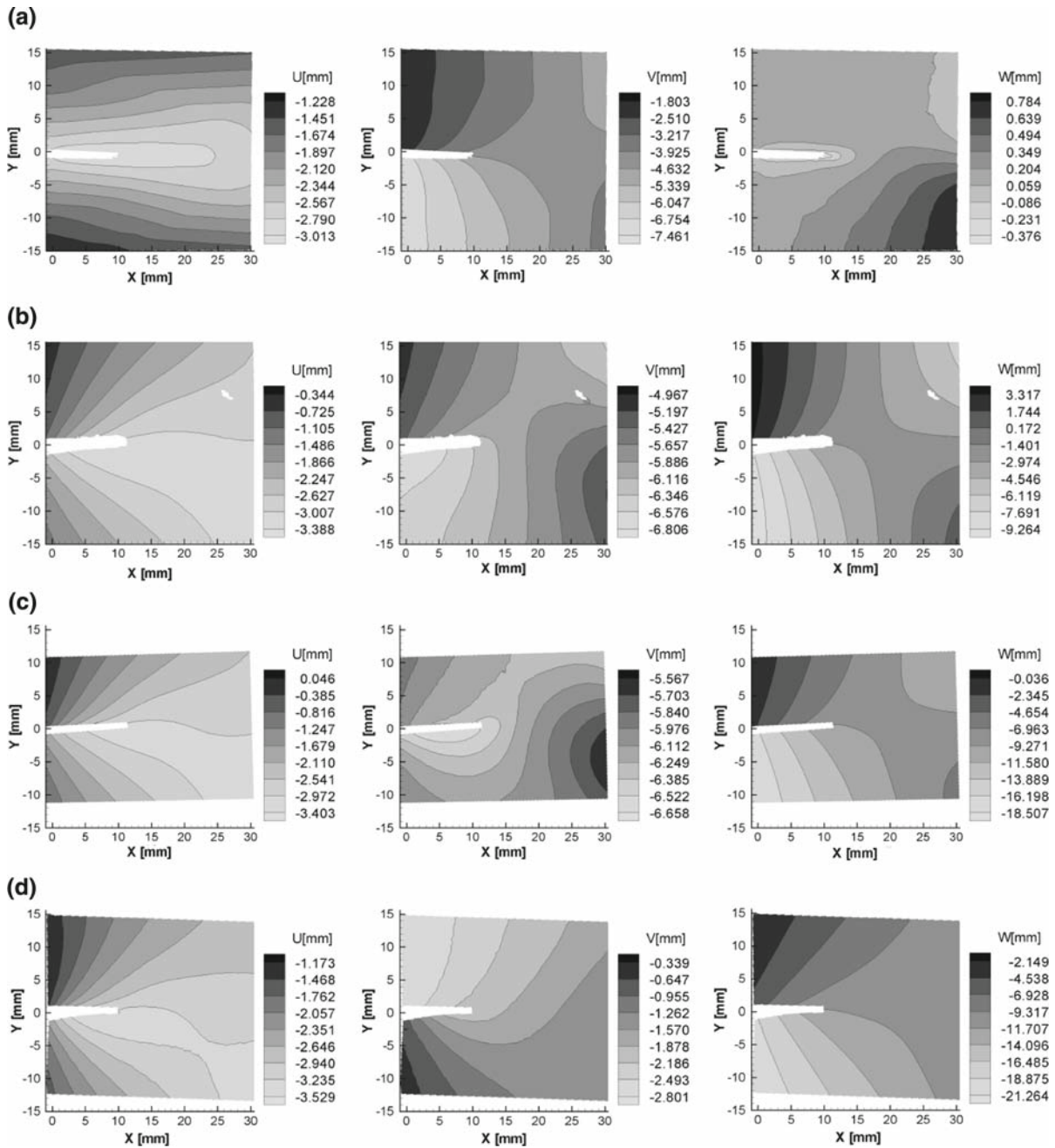
Fig. 7 Displacement contours in AL6061-T6 specimens under quasi-static loading at $\Phi = 0°, 30°, 60°$ and $90°$ during mixed mode I/III experiments, with various crack extension Δa.

a $\Phi = 0°$ $\Delta_a = 9.69\text{mm}$, **b** $\Phi = 30°$ $\Delta_a = 10.63\text{mm}$, **c** $\Phi = 60°$ $\Delta_a = 9.64\text{mm}$, **d** $\Phi = 90°$ $\Delta_a = 10.18\text{mm}$

the angle $\theta = 0°$ is along the X-axis. For comparison, the angular and radial variations of the surface strains for a stationary crack ($\Delta a = 0$ mm) are also presented in Fig. 11. It is seen that for each strain component

the amplitude of the strain for a growing crack is much larger than that for a stationary crack. For a given strain component, the functional form for the angular distribution at $r = 0.75$ mm and the radial distribution

Fig. 8 Displacement contours in GM6208 steel specimens under quasi-static loading at $\Phi = 0°$, $30°$, $60°$ and $90°$ during mixed mode I/III experiments, with various crack extension Δa.

a $\Phi = 0°$ $\Delta_a = 9.88$mm, **b** $\Phi = 30°$ $\Delta_a = 10.01$mm, **c** $\Phi = 60°$ $\Delta_a = 11.41$mm, **d** $\Phi = 90°$ $\Delta_a = 9.96$mm

at crack extensions $\Delta a > 0$ mm are approximately invariant with increasing crack extension. As shown in Fig. 12, the same trends are also observed in mixed I/III mode ($\Phi = 30°$, $60°$ and $90°$) AL6061-T6 specimens.

Figures 13 and 14 shows representative angular and radial variations for surface strains at various crack extensions with $\Phi = 0°$, $30°$, $60°$ and $90°$ in the AL6061-T6 and GM6208 steel specimens.
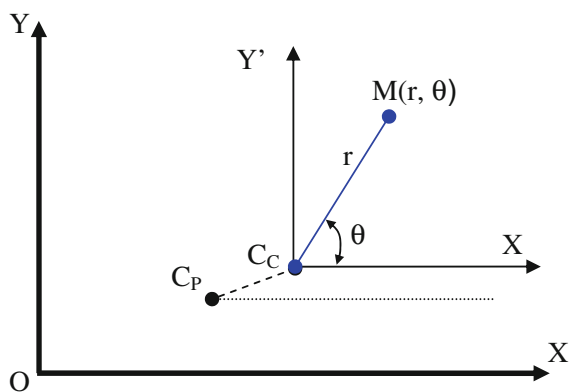
Fig. 9 The definition of a polar coordinate system (r, θ) with origin at the current crack tip Cc, where r is the radial distance between a point M and the current crack tip Cc, θ is the angle between lines CcX' and CcM. X'CcY' is the local Cartesian coordinate system with origin at the current crack tip Cc. XOY is the global Cartesian coordinate system, with origin O at the fatigue pre-crack tip and OX along the pre-crack direction. Cp is the previous crack tip position. All definitions are for the un-deformed configuration

3.4.1 Discussion

As shown in Fig. 10, the Mode I crack tip angular distributions of surface strains around a growing crack for aluminum alloy and steel specimens are very similar:

- $\varepsilon_{\theta\theta}$ has two minima and at least one maximum, ε_{rr} has a single minimum and two maxima, and $\varepsilon_{r\theta}$ has a single minimum and maximum.
- $\varepsilon_{\theta\theta}$ and ε_{rr} are almost symmetric with respect to $\theta = 0°$ (the X-axis direction), while $\varepsilon_{r\theta}$ is almost anti-symmetric relative to $\theta = 0°$.
- the angular locations of maxima in $\varepsilon_{\theta\theta}$ and minima in ε_{rr} are nearly the same, being qualitatively consistent with expectations based on plastic incompressibility.
- $\varepsilon_{\theta\theta}$ is the dominant strain component for a growing crack under mode I loading.

Consistent with the clear difference in ductility between the two materials (see Table 1) and the increased near-tip dimpling in the steel specimen (see Fig. 4), the near crack tip surface strain components in GM6208 steel are much larger than those in AL6061-T6. For example, just prior to fracture $(\varepsilon_{\theta\theta})_{\max}$ in steel is $2\times$ larger than that in aluminum alloy. In addition, the transition from minimum $\varepsilon_{r\theta}$ to maximum $\varepsilon_{r\theta}$ in steel is steeper than that in aluminum alloy. It is noted that the steel specimen has two tensile peaks in $\varepsilon_{\theta\theta}$ while aluminum

alloy has only one tensile peak in $\varepsilon_{\theta\theta}$, most likely due to the presence of slant crack growth in the aluminum alloy specimen, whereas the steel specimen undergoes nominally planar crack growth in the presence of large through-thickness dimpling.

The radial distribution along the angle θ corresponding to a local maximum in the strain component of interest is shown in Fig. 11b for the aluminum alloy specimen. The measured trend is qualitatively consistent with the expected inverse power law form $r^{-\beta}$. However, the measured radial distributions for ε_{rr} and $\varepsilon_{\theta r}$ along the specified angle θ indicate that they increase only slightly with decreasing radial distance to the growing crack tip. The form of the radial distributions in steel specimen as shown in Fig. 14b is similar, even along different angles.

For mixed mode I/III loading ($\Phi = 30°$, $60°$ and $90°$), Figs. 13a and 14a show the angular distributions for aluminum alloy and steel specimens, respectively. Results for a growing crack indicate that all mixed-mode I/III loading cases ($\Phi = 30°$, $60°$ and $90°$) have almost identical angular distributions, with (a) a single positive and negative maximum in each strain component, (b) the maxima in the components occur at different θ, with $\varepsilon_{\theta\theta}$ maximum located at $\theta \approx 0°$ and maxima in ε_{rr} and $\varepsilon_{\theta r}$ located at $\theta > 0°$ and (c) the magnitudes of strain maxima are in the order $\varepsilon_{\theta\theta} > \varepsilon_{rr} > \varepsilon_{\theta r}$.

Direct comparison of measured data in Figs. 13a and 14a demonstrates that the angular distributions under combined in-plane and out-of-plane loading are different from those for the nominally Mode I loading case. In particular, there is only one positive maximum in each of the strain components during mixed-mode I/III loading. Furthermore, the symmetry observed in the angular distributions for mode I loading has been modified by the mode III loading component. For mixed mode I/III loading, (a) $\varepsilon_{\theta\theta}$ and ε_{rr} are no longer symmetric with respect to $\theta = 0°$ (the X-axis direction), (b) $\varepsilon_{r\theta}$ is not anti-symmetric relative to $\theta = 0°$ in the angular distribution of $\varepsilon_{\theta\theta}$, with large tensile residual strain measured near the crack upper wake (connected to the fixed grip), while slightly small compressive residual strains are observed near the crack lower wake (connected to the moving grip). The angular locations of minimum in $\varepsilon_{\theta\theta}$ and maximum in ε_{rr} are nearly the same, with the location of minimum in ε_{rr} is about $-20°$ off the location of maximum in $\varepsilon_{\theta\theta}$.

Comparisons of the radial distributions along the direction of the strain maxima shown in Figs 13b and

Fig. 10 Angular variations of surface strains as a function of the radial distance r from the current crack tip (in the un-deformed configuration) in mode I ($\Phi = 0°$) experiments of an AL6061-T6 specimen and a GM6208 steel specimen, where the angle $\theta = 0°$ is along the global X-direction **a** $\Phi = 0°$ at $\Delta_a = 8.01$mm for AA 60601, **b** $\Phi = 0°$ at $\Delta_a = 3.85$mm for GM 6208
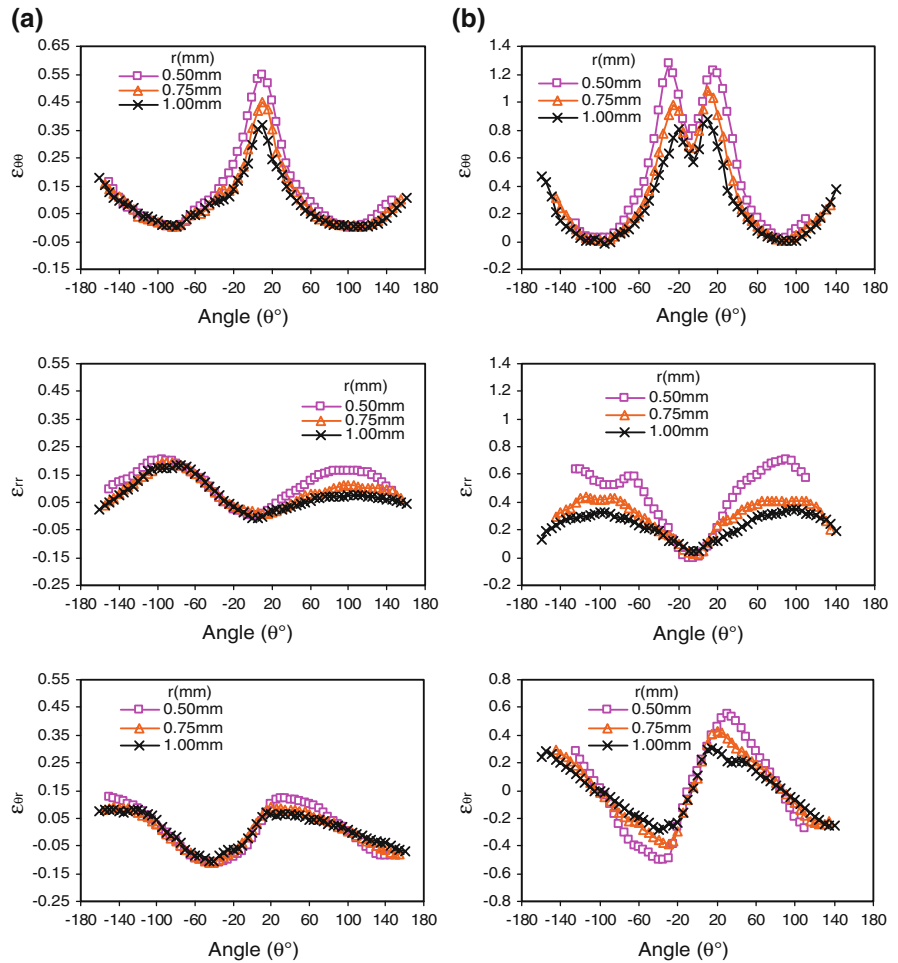
14b indicate that mode mixity has a small effect on the overall radial trends for each strain component. It is also seen that at a given radial distance ahead of the growing crack, mode I loading will introduce greater $\varepsilon_{\theta\theta}$ than the mixed mode I/III loading. However, $\varepsilon_{\theta\theta}$ increases more rapidly in mixed mode I/III loading than in mode I loading as the radial radial distance goes to zero (r → 0), which implies mixed mode I/III loading has more localized hoop strain $\varepsilon_{\theta\theta}$ ahead of the growing crack.

The radial variations of surface strains shown in Figs. 13 and 14 indicate that the strain component $\varepsilon_{\theta\theta}$ increases sharply as the distance from crack tip r → 0, suggesting a strain singularity near the crack tip in both materials. For all loading angles, Fig. 15 presents a typical natural log–log plots of the near-tip tensile $\varepsilon_{\theta\theta}$ as a function of r for 0 < r ≤ 1.2 mm. As shown in Fig. 15, the data in a portion of the crack tip region is reasonably represented by a linear fit. The slopes obtained by least square fitting to the data are also presented in Fig. 15.

Figure 15 indicates that the hoop strain component $\varepsilon_{\theta\theta}$ has a power-law type strain singularity near the crack tip in pure tension and mixed mode I/III loading for AL6061-T6 and GM6208 steel, respectively. For the aluminum alloy and steel specimens, the well-defined linear trends clearly show that the measured surface singularity in mixed mode I/III is higher than that in mode I. Further analyses shows that the natural logarithmic function ln(1/r) fits the ε_{yy} strain distribution for both materials equally well.

3.5 COD results

COD is an important parameter often used to predict fracture in a wide range of ductile materials (Dawicke and Sutton 1994; Dawicke et al. 1995; Ma et al. 1999; Newman et al. 2003; Sutton et al. 2000a,b). The procedure to assess the COD variation under mixed mode I/III loading with severe out-of-plane

Fig. 11 Angular and radial variations of surface strains as a function of crack extension Δa in a mode I ($\Phi = 0°$) AL6061-T6 specimen, where r is the radial distance from the current crack tip (in the un-deformed configuration), and the angle $\theta = 0°$ is along the global X-direction. **a** Angular variations at $r = 0.75$ mm from current crack tip, **b** Radial variation along $\theta = 0°$
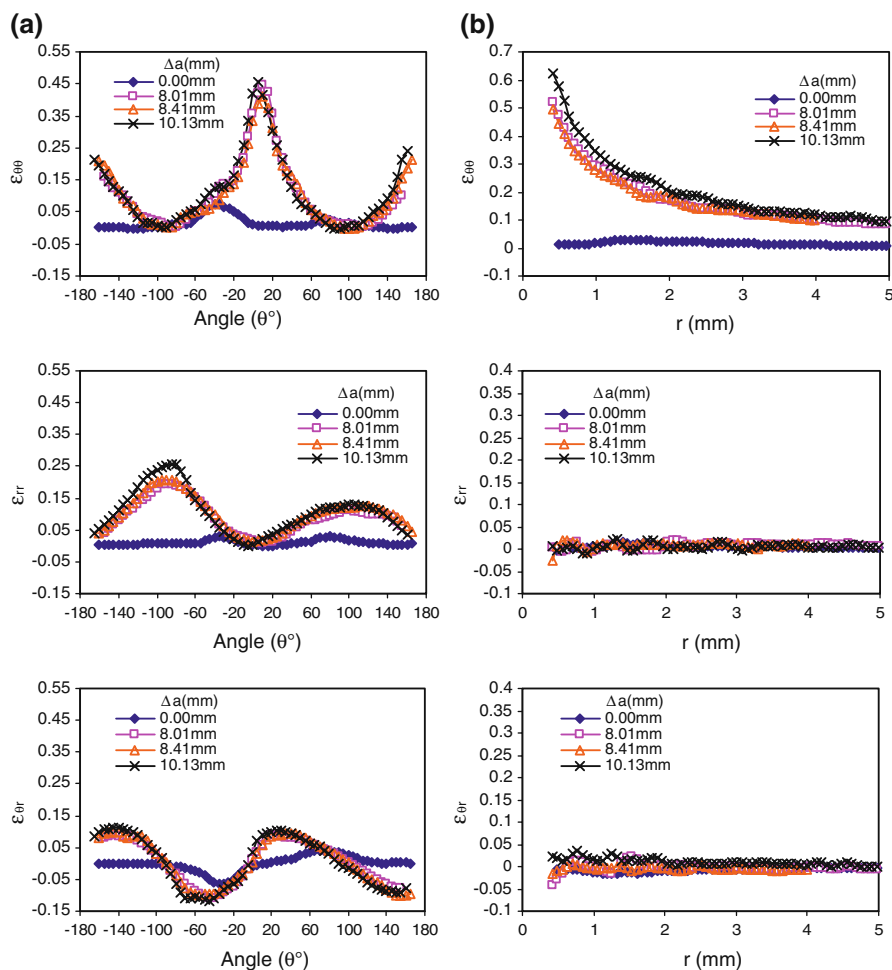

deformation by using 3D DIC was outlined previously (Sutton et al. 2007). Following the procedure, COD measurements were conducted for 2 mm thick AL6061-T6 and GM6208 steel specimens during crack growth with mixed mode I/III loading at $\Phi = 0°, 30°, 60°$ and $90°$.

Figure 16 shows typical variations of COD components and total COD under mixed mode I/III loading at $\Phi = 90°$ for AL6061-T6 and GM6208 steel specimens, along with a compilation for the average COD and the standard deviation in COD and its components. Similar trends are observed in mixed mode I/III loading at $\Phi = 30°$ and $60°$ for both steel and aluminum alloy. For all mixed mode cases ($\Phi > 0°$), when $\Delta a \geq t$, where $t = 2$ mm is the specimen thickness, it was observed that (a) all three COD components are present, (b) COD_{III} is the dominant component, COD_{II} is the smallest and $COD_I \approx 0.5\ COD_{III}$,

and (c) aluminum alloy and steel specimens have significantly different COD_{III} and COD_I components, as well as total COD values.

Figure 17 presents a compilation of all measured critical total COD $\left(COD = \sqrt{COD_I^2 + COD_{II}^2 + COD_{III}^2}\right)$ as a function of crack extension Δa for AL6061-T6 and GM6208 steel specimens under mixed mode I/III loading at $\Phi = 0°, 30°, 60°$ and $90°$. The stable critical COD values for Mode I loading ($\Phi = 0°$) shown in Fig. 17 are obtained from a series of mode I and mixed-mode I/II experiments on the same material, which were a part of the baseline study by the investigators. The setup for mixed mode I/II experiments and the procedure for measuring the corresponding COD can be found in the work by Dawicke and Sutton (1994) and Dawicke et al. (1995).

Fig. 12 Angular variations of surface strains as a function of crack extension in mixed I/III mode AL6061-T6 specimens, where $r = 0.75$ mm is the radial distance from the current crack tip (in the un-deformed configuration), and the angle $\theta = 0°$ is along the global X-direction. **a** $\Phi = 30°$, **b** $\Phi = 90°$
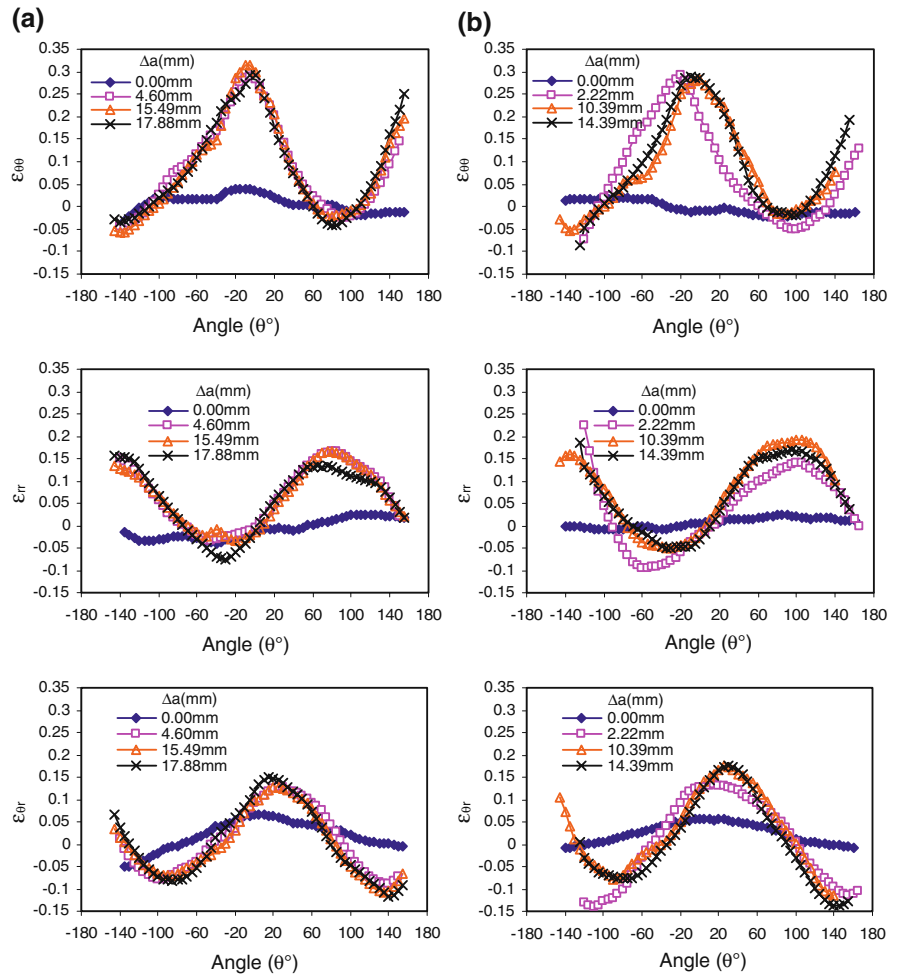

The following observations can be made from Figs. 16 and 17,

- There is a well defined transition in the early stage of crack growth ($\Delta a < t$), with the initially higher COD decreasing rapidly. For highly ductile materials, the initially higher COD values may be correlated with crack front phenomena such as crack blunting, crack tunneling and accumulation of damage during the initial stages of the fracture process.
- For all crack growth where $\Delta a > t$, the values for the COD components and total COD are nearly constant. These trends have been seen in a variety of fracture experiments.
- For both AL6061-T6 and GM6208 steel, stable COD data from different mixed mode I/III loading

angle $\Phi = 30°$, $60°$ and $90°$ fall in a well-defined band, which is clearly separated from Mode I COD data. These indicate that once the out-of-plane component (Mode III) is present during the loading process, additional increases in the out-of-plane loading do not have a significant effect on the mixed mode I/III stable COD values.

- For AL6061-T6, the mixed mode I/III average stable COD ≈ 0.40 mm is $4\times$ greater than the Mode I stable COD ≈ 0.10 mm. For steel specimen, the mixed mode I/III average stable COD ≈ 0.65 mm is about $3\times$ higher than the Mode I average stable COD ≈ 0.23 mm. These results indicate that the magnitude of the critical COD is a function of the type of mode mixity (i.e. whether the mixed mode involves a mode III component) in highly ductile,

Fig. 13 Angular and radial variations of surface strains as a function of crack extension in mode I ($\Phi = 0°$) and mixed I/III mode ($\Phi = 30°$, $60°$ and $90°$) AL6061-T6 specimens, where r is the radial distance from the current crack tip (in the un-deformed configuration), and the angle $\theta = 0°$ is along the global X-direction. **a** Angular variations at $r = 0.75$ mm, **b** Radial variations along $\theta = 0°$ (for $\Phi = 0°$ and $60°$), $-5°$ (for $\Phi = 30°$), or $-10°$ (for $\Phi = 90°$)
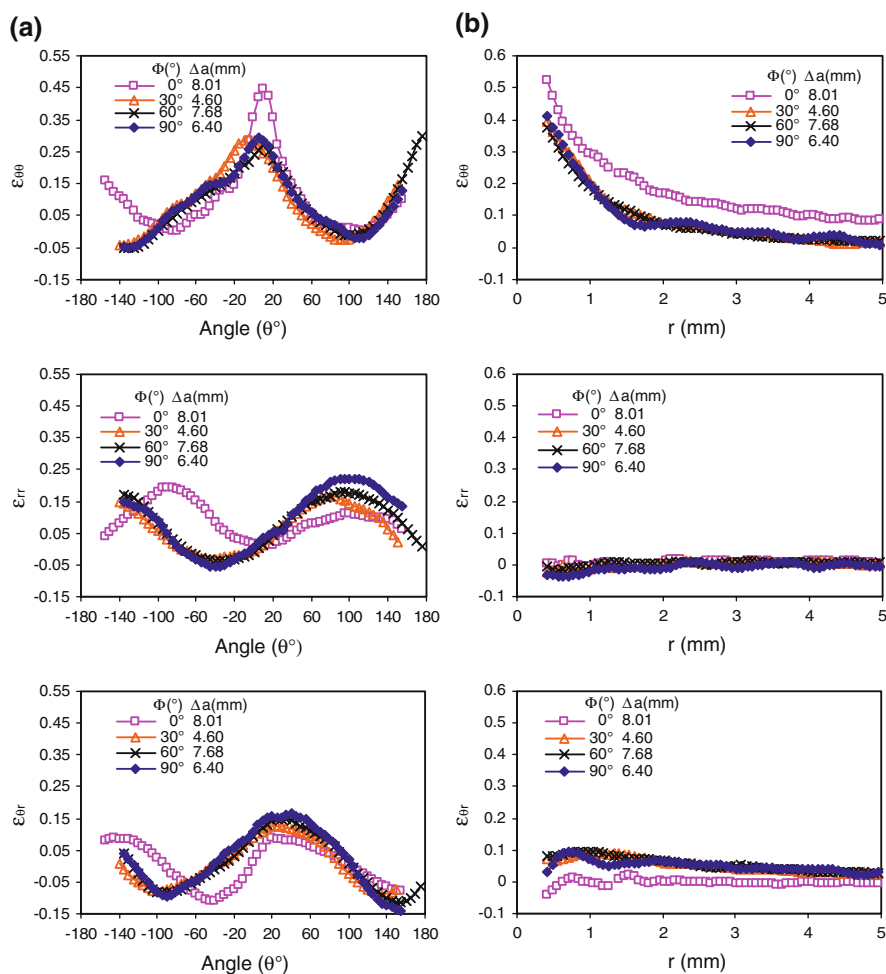
thin sheet materials. Though the precise reason for the large increase in COD is not fully understood, it is believed that the large structural, out-of-plane bending introduced by the mode III component in combined in-plane/out-of-plane loading contribute to the measured values of COD in these materials.

3.6 Discussion of results

There is a paucity of theoretical work for direct comparison to the measured angular variations in the polar strain components. For a stationary crack ($\Delta a = 0$ mm) under mode I loading, the measurements in AL6061-T6 and GM6208 steel can be compared with previous work by Hutchinson (1968) and Rice and Rosengren (1968), where the plastic stress and strain fields at a stationary crack tip were investigated under the assumption of small strain and deformation

plasticity. As shown in Figs. 13 and 14, the radial variations in $\varepsilon_{\theta\theta}$ and $\varepsilon_{\theta r}$ for a stationary crack in GM6208 steel under mode I loading are qualitatively similar to Hutchinson, Rice and Rosengren's (HRR) results, though the angular distributions in the polar strain components are different from what Hutchinson obtained. It is conjectured that intensive dimpling and crack slanting observed even before the crack growth in AL6061-T6 and GM6208 steel mode I loading specimens (Yan et al. 2007) are primarily responsible for the observed differences.

For angular field variations during crack growth under mode I loading in power hardening materials, Deng (1990) and Deng and Rosakis (1991, 1992a,b) performed detailed finite element simulations for both quasi-statically growing cracks and dynamically propagating cracks in elastic-plastic solids (elastic-perfect plastic materials, power hardening materials and

Fig. 14 Angular and radial variations of surface strains as a function of crack extension in mode I ($\Phi = 0°$) and mixed I/III mode ($\Phi = 30°$, $60°$ and $90°$) GM6208 steel specimens, where r is the radial distance from the current crack tip (in the un-deformed configuration), and the angle $\theta = 0°$ is along the global X-direction. **a** Angular variations at $r = 0.75$ mm, **b** Radial variation along $\theta = 0°$ (for $\Phi = 0°$ and $90°$), $-10°$ (for $\Phi = 30°$), or $-20°$ (for $\Phi = 60°$)
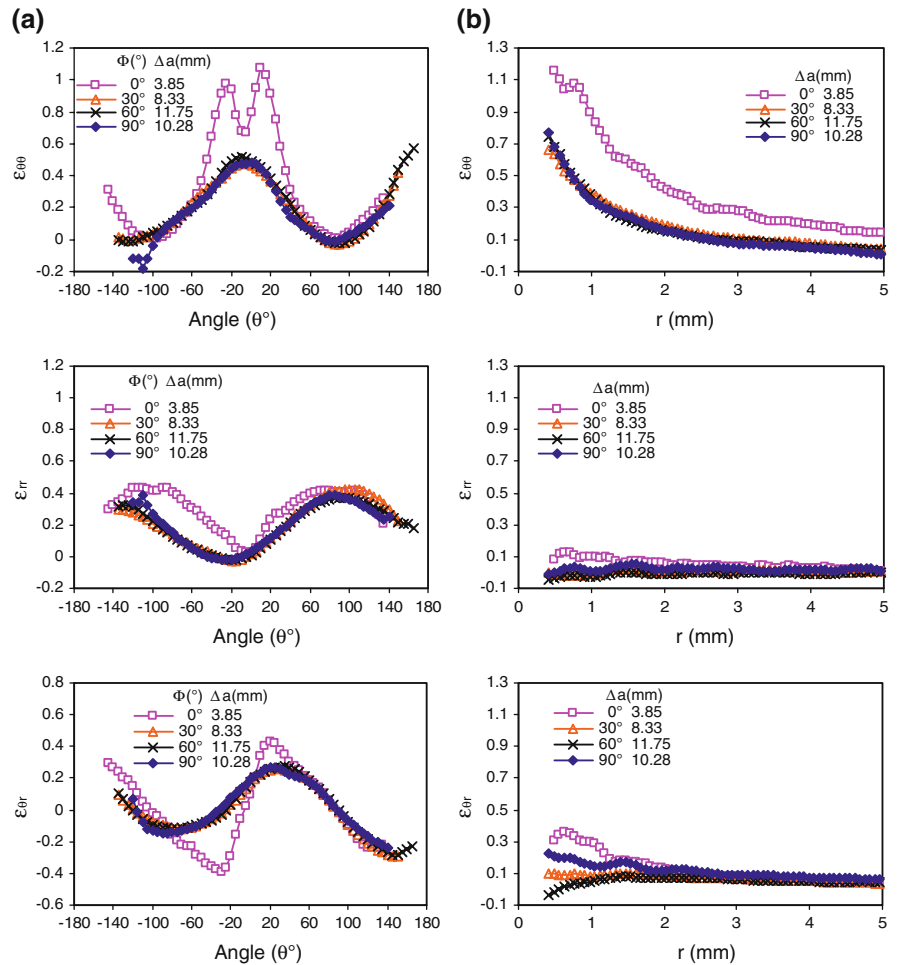

linear hardening materials), under mode I plane stress, small-scale yielding and steady-state conditions. For the elastic-perfect plastic materials, the in-plane polar strain components have a sinusoidal angular variation. AL6061-T6 aluminum alloy used in the current study has a large strain hardening exponent ($n = 13$, see Table 1) and thus behaves approximately similar to an elastic-perfectly plastic material. Comparison of results in Fig. 11 for growing crack in AL6061-T6 under mode I loading with those by Deng (1990) and Deng and Rosakis (1991, 1992a,b) for elastic-perfect plastic materials reveals that the overall trends for the angular variations in the two studies solutions are similar. This implies the strain hardening exponent does not have a significant effect on the functional form of the angular variation of polar strain components for growing cracks in ductile thin sheet materials under mode I loading.

For a growing crack under combined in-plane and out-of-plane loading, no report on the angular and radial variation of surface strains can be found in the open literature. As shown in Figs. 13a and 14a, for both AL6061-T6 and GM6208 steel under combined in-plane and out-of-plane loading ($\Phi = 30°$, $60°$ and $90°$), almost identical angular distributions of polar strain components for a growing crack were obtained. It is obvious that these angular variations were modified by the imposition of the mode III loading component, as discussed in Sect. 3.4. However, it is worth noting that for a given polar strain component, the overall shape of the crack tip angular variations under combined in-plane and out-of-plane loading is very similar to that under mode I loading despite the shift in the location of minimum/maximum or changes in symmetry. This may not be too surprising when one considers the non-negligible out-of-plane deformations observed under nominally mode I loading (see Fig. 4).

Figure 15 indicates that the measured surface singularity in tension-torsion loading is much stronger than
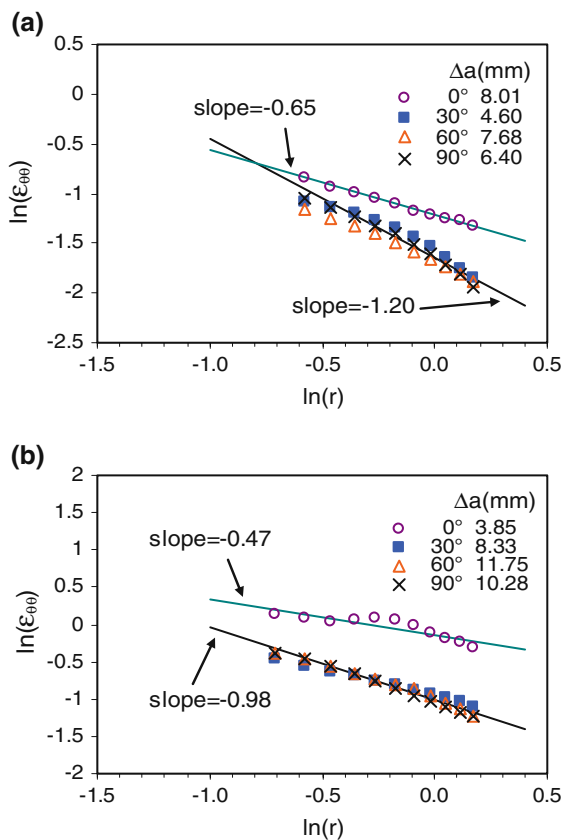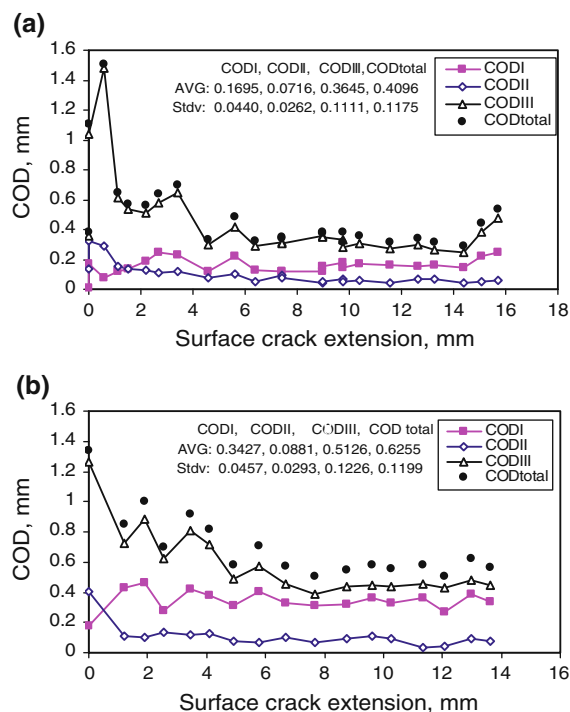
Fig. 15 $\ln(\varepsilon_{\theta\theta})$ versus $\ln(r)$ near the crack tip with radial distance from crack tip $r < 1.2$ mm for **a** AL6061-T6 specimens, **b** GM6208 specimens in mixed mode I/III experiments

Fig. 16 Typical variations of COD components and the total COD as a function of surface crack extension for **a** AL6061-T6 specimens, **b** GM6208 specimens loaded at $\Phi = 90°$ in mixed mode I/III experiments

that for tensile loading in both the steel and aluminum alloy specimens, demonstrating that at least one effect of combined mode I/III loading is to introduce the mode III loading component, which makes the strain field more localized. This need to be further investigated.

The COD results shown in Fig. 17 are consistent with our previously reported results (Sutton et al. 2007; Yan et al. 2007). The mixed mode I/III average stable COD for AL6061-T6 (GM6208 steel) is $4\times(3\times)$ greater than the Mode I and mixed-mode I/II stable COD. The increase of COD introduced by Mode III loading in the current study is much larger than that reported previously for another material (Sutton et al. 2001), where the measured critical COD for tension-torsion loading in AL2024-T3 is ∼18% larger than observed for in-plane tension and shear.

For mode I loading, it is well known that measured COD at the specimen surface in the early stage of crack growth ($\Delta a < t$) is much higher than the stable COD.

The initial higher COD values are believed to be related to crack tip blunting (Chan 1990). According to Newman et al. (2003), the initial higher value is traced back to the constraint effect in the crack front region and severe crack tunneling in the thin-sheet materials, though a quantitative correlation between COD and the crack tip strain field has not been established.

By comparing the radial variation of crack tip $\varepsilon_{\theta\theta}$ under mode I loading and under mixed mode I/III loading in Figs. 13 and 14 with the COD variation under mode I loading and under mixed mode I/III loading in Fig. 17, one observes that for a given material there seems to exist a correlation between variations in stable COD and that of the crack tip strain component $\varepsilon_{\theta\theta}$ during both crack initiation and SCG for different loading modes. During mode I loading, the larger and less singular crack tip strain component $\varepsilon_{\theta\theta}$ correlates with lower stable COD, while the lower and more singular crack tip component $\varepsilon_{\theta\theta}$ corresponds to higher stable COD under mixed mode I/III loading. It seems that the changes in the deformation fields around the crack front introduced by additional out-of-plane component form
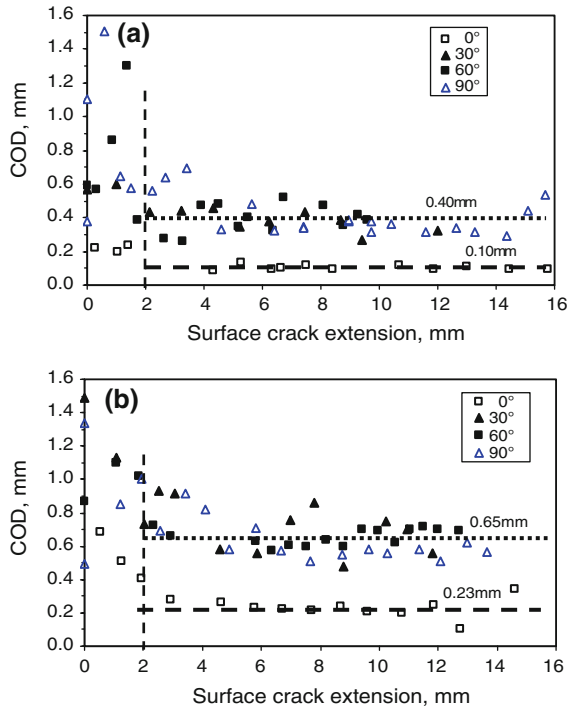
Fig. 17 Total COD variations as a function of surface crack extension for **a** AL6061-T6 specimens, **b** GM6208 specimens loaded at $\Phi = 0°$, $30°$, $60°$ and $90°$ in mixed mode I/III experiments

a basis for the increased critical CTOD value in mixed mode I/III. A full understanding of the effect of large out-of-plane structural bending on fracture prediction will require additional studies.

With regard to the utility of the COD measurement for stable tearing predictions, it is noted that Wei (2008) recently simulated the mixed mode I/III fracture events in thin sheet aluminum alloy and steel. The average values of the measured COD at 1 mm behind the moving crack front on the surface (see Fig. 17) were used to simulate crack extension and crack path for various mixed mode I/III events for both aluminum alloy and steel specimens. Results show that the COD based simulations are able to predict crack extension in thin-sheet specimens under remote mixed-mode I/III loading conditions. Furthermore, a bilinear representation for the measured COD can further improve the prediction by delaying initial crack growth until the measured COD occurs. In the mean time, the in-plane COD vector on the mid-plane of the specimen was utilized to determine crack path, and the predictions for all simulated cases match well with the experimental results, sug-

gesting that the crack path under local mixed-mode I/II/III conditions is controlled by the in-plane COD components.

4 Summary and concluding remarks

A series of mixed-mode I/III stable tearing experiments on highly ductile thin-sheet aluminum alloy and steel specimens have been performed. Using three-dimensional digital image correlation (3D-DIC) to measure the local crack tip fields and overall specimen deformations, features of crack growth in these mixed-mode I/III experiments are characterized, including (a) the specimen's deformed shape and 3D full-field surface displacement fields, (b) the load-crack extension curves and crack path, (c) angular and radial distribution of polar strain components, and (d) COD variation as a function of crack extension. The following conclusions are drawn from the experimental results:

(a) For both AL6061-T6 aluminum alloy and GM 6208 steel specimens under various mixed-mode I/III loading conditions ($\Phi = 30°$, $60°$ and $90°$), the growing crack tip fields have nearly identical angular and radial polar strain distributions. The measured strain fields are clearly different from those measured for the nominal Mode I loading case ($\Phi = 0°$).

(b) The introduction of a Mode III loading component lowers the value of the dominant strain component, $\varepsilon_{\theta\theta}$, ahead of the growing crack tip and increases the singularity of the strain as compared to that for the mode I case.

(c) For both AL6061-T6 and GM6208 steel, stable COD data from different mixed mode I/III loading angle $\Phi = 30°$, $60°$ and $90°$ fall in a well-defined band, which is clearly separated from Mode I COD data. The mixed mode I/III average stable COD value for AL6061-T6 (GM6208 steel) is $4\times$ ($3\times$) greater than the Mode I stable COD value.

References

Chan KS (1990) Crack-tip behavior of stationary and growing cracks in Al-Fe-X alloys: part I. Near-tip strain field. Metall Trans A 21A:69–80

Correlated Solutions, Inc (2007) VIC-2D and VIC-3D, 120 Kaminer way parkway suite A, Columbia, SC 29210. www.correlatedsolutions.com

Dawicke DS, Sutton MA (1994) CTOA and crack-tunneling measurements in thin sheet 2024-T3 aluminum alloy. Exp Mech 34(4):357–368

Dawicke DS, Sutton MA, Newman JC Jr et al (1995) Measurement and analysis of critical CTOA for thin-sheet aluminum alloy materials. In: Erdogan F (ed) Fracture mechanics 25, ASTM STP 1220, pp 358–79

Deng X (1990) Dynamic crack propagation in elastic-plastic solids. Ph.D dissertation, California Institute of Technology, Pasadena, California, May 1990

Deng X, Rosakis AJ (1991) Dynamic crack propagation in elastic-perfectly plastic solids under plane stress conditions. J Mech Phys Solids 39:683–722

Deng X, Rosakis AJ (1992a) A finite element investigation of quasi-static and dynamic asymptotic crack tip fields in hardening elastic-plastic solids under plane stress; part I: crack growth in linear hardening materials. Int J Fract 57:291–308

Deng X, Rosakis AJ (1992b) A finite element investigation of quasi-static and dynamic asymptotic crack tip fields in hardening elastic-plastic solids under plane stress; part II: crack growth in power-law hardening materials. Int J Fract 58:137–156

Gao X, Shih CF (1998) A parametric study of mixed-mode I/III ductile fracture in tough materials under small scale yielding. Eng Fract Mech 60(4):407–420

Hutchinson JW (1968) Plastic stress and strain fields at a crack tip. J Mech Phys Solids 16:337–347

Jones RH, Li H, Hirth JP (2001) Effect of mixed mode I/III loading on environment-induced cracking. Eng Fract Mech 68:789–801

Kamat SV, Hirth JP (1995) Mixed mode fracture toughness of engineering materials. J Engng Mater Technol 117(4):391–394

Kamat SV, Srinivas M, Rao PR (1998) Mixed mode I/III fracture toughness of armco iron. Acta Mater 46(14):4985–4992

Lan W, Deng X, Sutton MA et al (2006) Study of slant fracture in ductile materials. Int J Fract 141(3–4):469–496

Li H, Kurtz RJ, Jones RH (1998) Effect of thickness and loading mode on the fracture properties of V-4Cr-4Ti at room temperature. J Nucl Mater 258–263:1386–1391

Liu S, Chao YJ, Zhu X (2004) Tensile-shear transition in mixed mode I/III fracture. Int J Solids Struct 41:6147–6172

Ma F, Deng X, Sutton MA et al (1999) A CTOD-based mixed-mode fracture criterion. In: Miller KJ, McDowell DL (eds) Mixed-mode crack behavior, ASTM STP 1359. American Society for Testing and Materials, West Conshohocken pp 86–110

Ma L, Kobayashi AS, Atluri SN et al (2002) Crack linkup: an experimental analysis. Exp Mech 42(2):147–152

Newman Jr JC, James MA, Zerbst U (2003) A review of the CTOA/CTOD fracture criterion. Eng Fract Mech 70:371–385

Pan J (1990) Asymptotic analysis of a crack in a power-law material under combined in-plane and out-of-plane shear loading conditions. J Mech Phys Solids 38(2):133–159

Pan J, Shih CF (1992) Elastic-plastic analysis of combined mode I, II and III crack-tip fields under small-scale yielding conditions. Int J Solids Struct 29(22):2795–2814

Paterson EA, Gungor S (1997) A photoelastic study of an angle crack specimen subject to mixed mode I-III displacements. Eng Fract Mech 56(6):767–778

Rice JR, Rosengren GF (1968) Plane strain deformation near a crack tip in a power law hardening material. J Mech Phys Solids 16:13–31

Sutton MA, Boone ML, Ma F, Helm JD (2000a) A combined modeling-experimental study of the crack opening displacement fracture criterion for characterization of stable crack growth under mode I/II loading in thin sheet materials. Eng Fract Mech 66:171–185

Sutton MA, Deng X, Ma F et al (2000b) Development and application of a crack tip opening displacement-based mixed mode fracture criterion. Int J Solids Struct 37:3591–3618

Sutton MA, Helm JD, Boone ML (2001) Experimental study of crack growth in thin sheet material under tension-torsion loading. Int J Fract 109:285–301

Sutton MA, Yan J-H, Deng X, Cheng C-S, Zavattieri P (2007) Three-dimensional digital image correlation to quantify deformation and crack-opening displacement in ductile aluminum under mixed-mode I/III loading. Opt Eng 46(5):051003

Wei Z, Yan J, Deng X et al (2005) Study of mixed-mode I/III fracture in ductile materials. In: Proceedings of the 2005 SEM annual conference and exposition on experimental and applied mechanics, 1651–1655, Portland, Oregon, June 7–9, 2005

Wei Z (2008) Study of fracture in ductile thin sheets under remote I/III loadings. Ph.D dissertation, University of South Carolina, Columbia South Carolina, June 2008

Yan J-H, Sutton MA, Deng X, Cheng C-S (2007) Mixed-mode fracture of ductile thin-sheet materials under combined in-plane and out-of-plane loading. Int J Fract 144:297–321

Zucchini A, Hui CY, Zehnder Alan T (2000) Crack tip stress fields for thin, cracked plates in bending, shear and twisting: a comparison of plate theory and three-dimensional elasticity theory solutions. Int J Fract 104:387–407